Journal of Microelectronics and Electronic Packaging (2024) **21**, 73–79
Copyright © International Microelectronics Assembly and Packaging Society
ISSN: 1551-4897

Investigation of Ohmic Contacts and Resistances of a 4H-SiC CMOS Technology up to 550°C

Mathias Rommel*, Alexander May, Leander Baier, Julian Kauth, Norman Böttcher, and Michael Jank

***Abstract*—In this work, the temperature dependence of all relevant resistances of a 4H-SiC CMOS technology for high-temperature applications is investigated from room temperature up to 550°C. This includes sheet resistances (R_{sh}) of differently doped regions, metallization layers (Ti/Pt and Ti/Pt/Ti layer stacks), and highly n-doped polycrystalline silicon as well as specific contact resistivity (ρ_c) to highly n- and p-doped 4H-SiC obtained by N and Al implantation, respectively. Different test structures were used for comparison and consistency of the results. Positive temperature coefficients of resistance were observed for the metallization layers (2,700 ppm/K) and for highly n-doped polycrystalline silicon (1,360 ppm/K). R_{sh} and ρ_c for highly n-doped 4H-SiC regions show only moderate variation with temperature whereas a rather strong decrease of R_{sh} and ρ_c can be observed for highly p-doped 4H-SiC and of R_{sh} for moderately p-doped 4H-SiC from room temperature up to 200°C which is mainly due to incomplete ionization of Al-doped regions. For implanted regions, modeled $R_{sh}(T)$ data qualitatively confirm measured results.**

***Keywords*—4H-SiC, CMOS, temperature dependence, ohmic resistance, sheet resistance, specific contact resistivity**

Introduction

Recently, a high-temperature compatible 4H-SiC-CMOS technology was introduced targeting applications for temperatures above 500°C [1, 2]. This technology also allows designing and realizing more complex circuits such as a 64-pixel UV sensor array with integrated readout circuitry [3]. The technology is also accessible via the EUROPRACTICE IC foundry service as an early access prototype technology [4]. To support IC design, a preliminary process design kit is available which, among other supporting information, includes Verilog-A compact models and scalable n-channel and p-channel metal-oxide-semiconductor transistor (NMOS and PMOS, respectively) parameterized cells.

However, models for passive components are not available yet, although accurate knowledge of the temperature dependence of their electrical characteristics is essential for precise circuit design. Next to capacitive elements, particularly ohmic elements such as resistors, wire routing, contacts to semiconductor regions as well as differently doped semiconductor regions need to be considered. The latter will be investigated in this work addressing a temperature range from room temperature to 550°C. Different types of test structures will be used to characterize Ti/Al-based and NiAl-based ohmic contacts on p- and n-doped 4H-SiC, respectively, with contact areas ranging between $(3\ \mu m)^2$ and $(100\ \mu m)^2$, sheet resistances of implanted regions, such as highly n- and p-doped contact implants as well as p-doped well regions. Finally, the sheet resistance of highly n-doped polycrystalline silicon (polySi) and metallization layers will be considered.

The manuscript was received on July 24, 2024; revision received on September 25, 2024; accepted on October 2, 2024.

The original version of this paper was presented at the IMAPS International Conference and Exhibition High Temperature Electronics Network (HiTEN 2024) in Edinburgh, Scotland, United Kingdom on July 15-17, 2024.

Fraunhofer Institute for Integrated Systems and Device Technology IISB, Schottkystraße 10, Erlangen, Germany

*Corresponding author; email: mathias.rommel@iisb.fraunhofer.de

Experimental and Evaluation

A. Sample Preparation

The investigated samples were fabricated at Fraunhofer IISB using their prototype 2 µm HT CMOS technology. In this work, the following test structures were investigated for evaluating relevant ohmic resistances: meander type resistors (MEA) to evaluate sheet resistances (R_{sh}), cross-bridge kelvin resistors (CBKR) to determine specific contact resistivity (ρ_c), and transfer length method (TLM, also known as transmission line model) structures to analyze R_{sh}, ρ_c, and transfer length (L_T) [5]. For all investigations, test structures from different chips from an exemplary wafer were analyzed and indicated by ascending number (e.g., MEA #1 – MEA #3).

The detailed process flow for the CMOS process is described in our previous work [1]. The main process steps relevant to the preparation of the investigated test structures are summarized hereafter. First, a 12-µm thick epitaxial layer with an N doping concentration of 5×10^{15} cm^{-3} was grown by chemical vapor deposition on commercially obtained 150 mm 4H-SiC substrates with a specific resistivity of 15-28 mΩcm. Next, locally doped contact and well regions were defined by implantation using N for n-doping and Al for p-doping. Subsequent high-temperature activation and annealing process at 1,700°C for 30 min in Ar atmosphere is followed by the removal of the carbon capping layer used for protecting the SiC surface during annealing [6]. The last steps of the carbon capping layer removal include a sacrificial thermal oxidation of about 10 nm thickness.

In the following, the implanted regions are referred to as n^+ and p^+ for highly doped contact regions to n- and p-doped 4H-SiC, respectively, and as nwell and pwell for the moderately doped well regions defining the channel doping of n- and p-MOSFETs, respectively. For all according test structures, n^+-implanted regions were always embedded in a pwell region and p^+-implanted regions in a nwell or pwell region,

depending on the actual structure. Note that the implanted regions of the TLM structures underwent an additional thermal oxidation step resulting in a 55-nm thick SiO_2 consuming approximately 25 nm of SiC. This equally thins the implanted doping profiles in the TLM structures. In the contact areas, this oxide was removed before contact formation. For both, MEA and TLM pwell test structures, a p^+ implantation was performed below the contact regions to ensure proper ohmic contacts.

A 1,050°C temperature step formed dedicated Ni_2Si n-type and Ti_3SiC_2 p-type ohmic contacts after metal deposition and patterning. First metal layer (M1) consists of an evaporated stack of 40 nm Ti and 400 nm Pt, whereas the second one (M2) has an additional evaporated layer of 40 nm Ti on top of the Pt.

Highly n-doped polysilicon (polySi) is used as a gate electrode and possible routing material in the investigated CMOS technology. Thus, MEA test structures were used to evaluate polySi, M1 and M2. These MEA test structures were isolated with thick SiO_x toward SiC.

B. Measurements and Evaluation

All above-mentioned test structures were characterized by current-voltage (I-V) measurements from room temperature up to 550°C. Electrical characterization was performed with a high-temperature probing setup in an ambient atmosphere. This setup consists of a SUSS PM5 probe station, the Keithley SCS-4200 with three 4200 source measure units (SMU) and one 4210-SMU, a 630 W hotplate up to 650°C from G. MAIER Elektrotechnik GmbH with an accuracy of ±5 K in the investigated temperature range due to the self-built setup together with manipulators and tungsten probe tips for high temperature probing from Signatone Corporation. MEA resistors were measured using four-terminal sensing with two SMUs on each contact pad. The M1 and M2 ones were measured from −0.1 V to +0.1 V in 10 mV steps, the polySi resistors as well as those for the doped SiC regions from −1 V to +1 V in 100 mV steps. CBKR structures were measured from −1 V to +1 V in 50 mV steps with one or two SMU connected with each pad to achieve four-terminal sensing. To ensure proper measurement results and structure fidelity, all CBKR structures were measured twice by changing the terminals for forcing current and measuring voltage [7]. If consistent, results were averaged from both measurements for evaluation. Fig. 1 exemplarily shows the temperature-dependent I-V measurements of CBKR structures with contact sizes of $(6\ \mu m)^2$ for both, n^+ and p^+: All I-V curves exhibit a high linearity.

TLM structures were also measured from −1 V to +1 V in 100 mV steps using four-terminal sensing with one SMU on each pad. All resistances determined from *I-V* measurements were only considered for further evaluation if the calculated coefficient of determination (R^2) was larger than .997.

MEA test structures were investigated for n^+, p^+, pwell, polySi, M1, and M2. All MEA designs share the same geometry with 110.7 squares, each with nominal 12 µm side length, connecting the contact pads. Included are 14 corner squares, which have a reduced effective square length of 55% [8]. This results in an effective length of 110.7 squares. Investigated CBKR test structures for both n^+ and p^+ have squared contacts with side lengths ranging from 3 to 10 µm in 1 µm intervals to include investigation of quality and fidelity of rather small ohmic contacts, which are known to affect ρ_c of p-type ones [9]. TLM test structures for n^+, p^+, and pwell regions have squared contacts with a side length (W) of 100 µm and distances of 15, 30, 60, 120, and 240 µm between individual contacts.

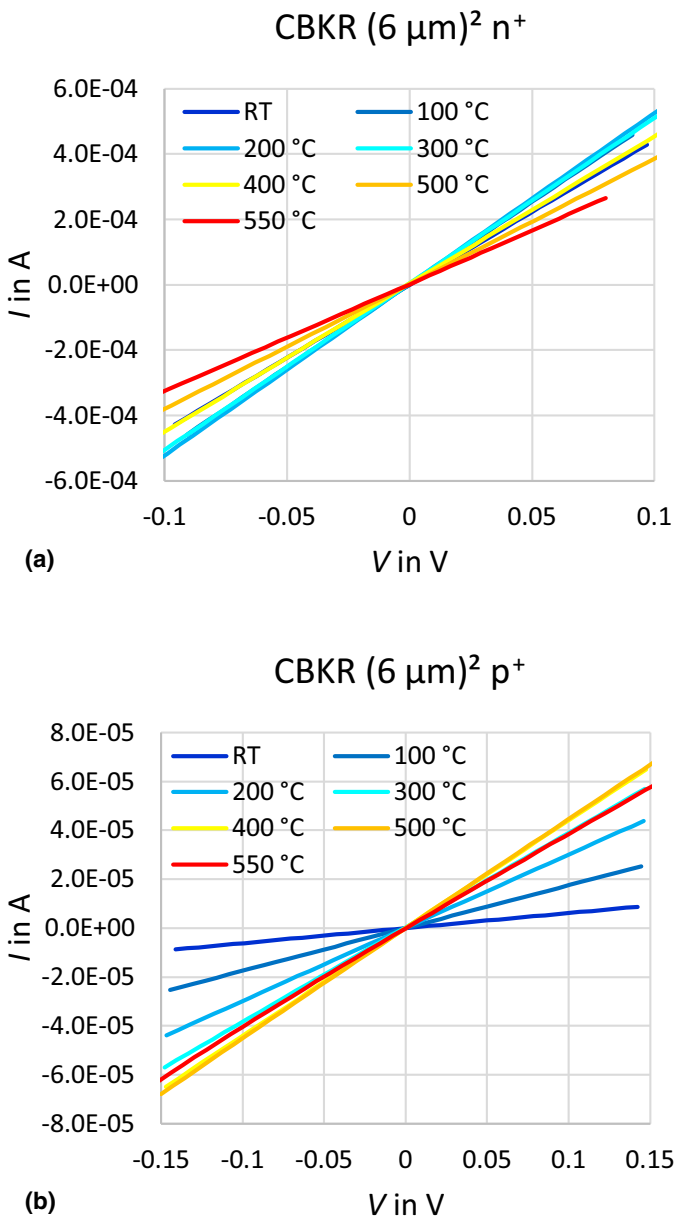

Fig. 1. Temperature-dependent I-V measurements of CBKR structures (contact size: $(6\ \mu m)^2$) for (a) n^+ and (b) p^+.

Evaluation of TLM structures was performed by evaluating the resistance versus contact pad distance (d) plot, as exemplarily depicted in Fig. 2 and as described in literature [5]. Please, note that the contact resistance R_C from TLM measurements is defined as half the intercept between the regression line and the R-axis, whereas L_T is obtained from the intercept between the regression line and the d-axis [5]. From those parameters together with the given W, the specific contact resistivity (ρ_c) can be calculated using equation (1) [5]. For the determination

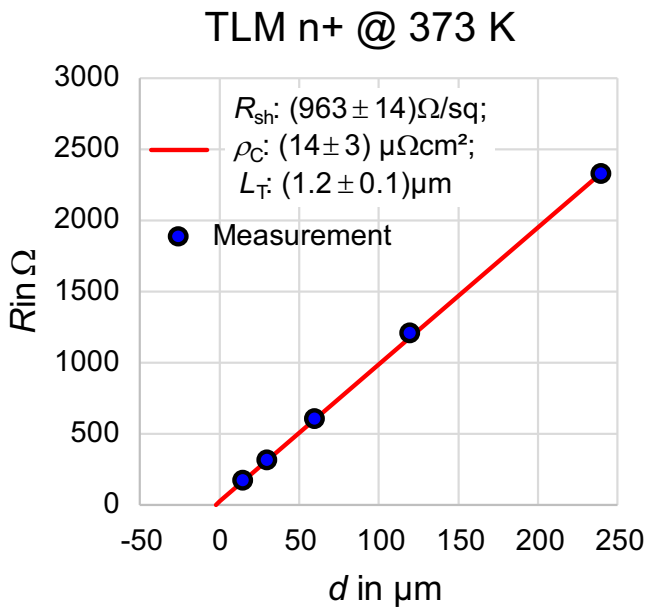

Fig. 2. Exemplary R(d) plot of a TLM test structure for characterization of an n^+ region at 373 K; the legend of the regression line shows evaluated parameter values.

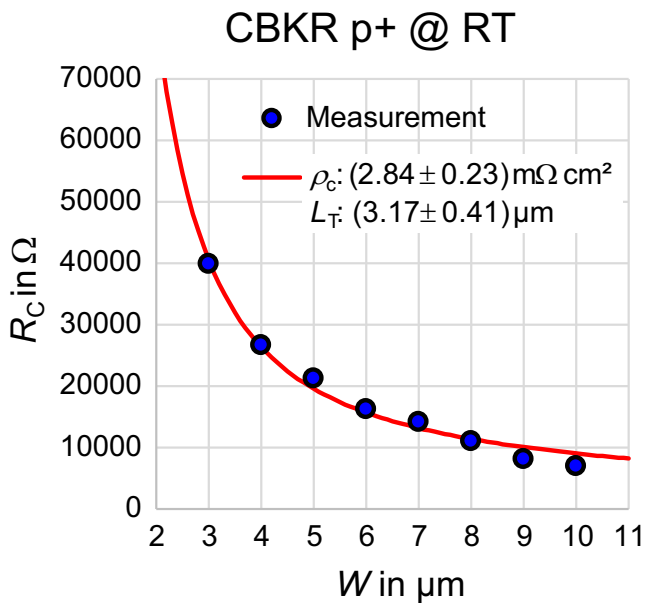

Fig. 3. Exemplary contact resistance versus contact side length W for CBKR test structure for characterization of contacts on a p^+ region at room temperature (RT); the legend of the line fitted according to equation (1) shows evaluated parameter values.

of the uncertainty of sheet resistance (R_{sh}), ρ_c, and transfer length (L_T), systematic error propagation was performed. For all test structures, the condition $W \geq L_T$ was fulfilled which simplifies equation (1) used within the TLM evaluation procedure. Only R_{sh} was evaluated from the pwell TLM test structures as contact resistances were too small in comparison with the sheet resistances due to the p^+ contact implantation used.

For CBKR square contacts with side lengths W, ρ_c and L_T were determined by fitting equation (1) [5] to the measured contact resistances (R_C) as exemplarily shown in Fig. 3

$$R_C = \frac{\rho_C}{L_T W} \coth\left(\frac{W}{L_T}\right). \quad (1)$$

The temperature dependence of MEA resistors for polySi as well as M1 and M2 was evaluated by determining the temperature coefficient of resistance (α) according to equation (2) with the reference temperature (T_0, in this work approximately 298 K) and measurement temperature (T) [10]

$$R_{sh} = R_{sh}(T_0)\ (1 + \alpha\ (T - T_0)). \quad (2)$$

C. Modeling of Sheet Resistances of Doped 4H-SiC

Theoretical calculations of the sheet resistances were compared with experimental data for the three investigated regions n^+, p^+, and pwell, respectively. The sheet resistance fundamentally depends on the free charge carrier concentration, their mobilities and the thickness of the implanted layer [5]. For 4H-SiC, incomplete ionization needs to be accounted for considering two different ionization energies (E_{D1}, E_{D2}) and (E_{A1}, E_{A2}) for both, N and Al, respectively. The effective nominal doping concentrations of N and Al (N_N and N_{Al}) were assumed to be evenly distributed between the two energy levels. N_N and N_{Al} as well as the thicknesses of the implanted layers (t_{imp}) were approximated from the actual doping profiles given in May et al. [6].

Electron or hole concentrations (n or p, respectively) were calculated by solving the neutrality equation. For the p-type regions where doping was obtained by ion implantation and subsequent high-temperature annealing, compensation needs to be considered [11] and, thus, the neutrality equation was solved with an additional concentration of compensating defects (N_{comp}). The parameters used for modeling $R_{sh}(T)$ data for n^+, p^+, and pwell regions are summarized in Table I.

Hole mobilities (μ_p) were calculated by considering scattering by ionized impurities, neutral impurities, acoustic phonons, nonpolar optical phonons, and polar optical phonons as described in the literature [12, 13]. Electron mobilities (μ_n) were modeled following the empirical approach given by [14]. R_{sh} was then calculated according to equation (3) with the elementary charge (q)

$$R_{sh} = \left(q\ t_{imp}\left(n\ \mu_n + p\ \mu_p\right)\right)^{-1}. \quad (3)$$

Table I
Parameters for Obtaining Modeled $R_{sh}(T)$ Curves Are Presented in Fig. 4 for n^+, p^+, and pwell Regions. N_{imp} Stands for N_N and N_{Al}, Respectively; $E_{1,2}$ Stands for E_{D1}, E_{D2} or E_{A1}, E_{A2}

	n^+	p^+	pwell
N_{imp} in cm^{-3}	5.0×10^{19}	3.5×10^{19}	2.0×10^{17}
$E_{1,2}$ in meV	61, 126 [15]	162, 260 [12]	214, 399[a]
N_{comp} in cm^{-3}	—	1.8×10^{18}	8×10^{16}
t_{imp} in nm	200	130	600

[a]The exact values of E_{A1} and E_{A2} used here for pwell were recently determined from the evaluation of Hall measurements on comparable samples by simultaneously fitting carrier concentration and mobility [13] which will be published elsewhere. They are, however, in very good agreement with values from the literature [11] for similar samples.

Results and Discussion

Geometrical dimensions of TLM structures (and here, especially the width of the contacts as well as the widths of the implanted regions) are much larger than those of MEA and CBKR structures. Thus, results from MEA and CBKR structures are more affected by small deviations from nominal geometrical dimensions. This has to be considered when comparing measurement results from the different test structures.

To check consistency and comparability of R_{sh} results for the implanted regions n^+, p^+, and pwell as well as of ρ_c results for the ohmic contacts on both, n^+ and p^+ regions, results from different test structure types are compared, i.e.,: for R_{sh}, results from TLM and MEA, and for ρ_c, results from TLM and CBKR test structures are compared.

A. Sheet Resistance of Implanted Regions

Evaluated R_{sh} results for the implanted regions n^+, p^+, and pwell from TLM and MEA test structures are presented in Fig. 4 as a function of measurement temperature together with modeled sheet resistances.

Compared with results from MEA resistors, results from TLM structures are by approximately 14% ± 2% larger for n^+, 20% ± 5% for p^+, and 10% ± 3% for pwell regions. In a good approximation, this can be directly related to the removal of the first 25 nm of the implantation profile for the TLM structures by thermal oxidation as described above: Multiplying the TLM R_{sh} values by the factor $(t_{imp} - 25\ nm)/t_{imp}$ with t_{imp} as given in Table I would lead to 12% smaller TLM R_{sh} values for n^+, 24% smaller for p^+, and 4% smaller values for pwell regions, leading to a very good agreement between TLM and MEA R_{sh} data.

The temperature dependence of the modeled sheet resistances shows a very similar trend as measured data for all regions with a slightly larger deviation for the n^+ region. Absolute values of the modeled curve are always higher than measured data but still a good agreement can be concluded, especially for the p^+ region. The difference between the absolute values of modeled and measured data is at least partly due to the approximations used to calculate the modeled curves, e.g., assumption of a box type implantation profile with approximated N_{imp} and t_{imp}.

B. Specific Contact Resistivity of Implanted Regions

Fig. 5 presents ρ_c results for the implanted regions n^+ and p^+ from TLM and CBKR test structures as a function of measurement temperature, whereas Fig. 6 presents corresponding L_T data. For the contacts on n^+ regions, simultaneous fitting of both ρ_C and L_T to the measured CBKR data allows different combinations of ρ_C and L_T with reasonable fits. Thus, the presented CBKR results for n^+ were obtained with a fixed L_T of 1.2 µm which is in good agreement with the L_T data obtained from according TLM evaluation displayed in Fig. 6a.

Absolute values of ρ_c on n^+ regions are comparable with typical data from the literature [16]. As an example, even for small contact areas of $(4\ \mu m)^2$ and MEA resistors with five

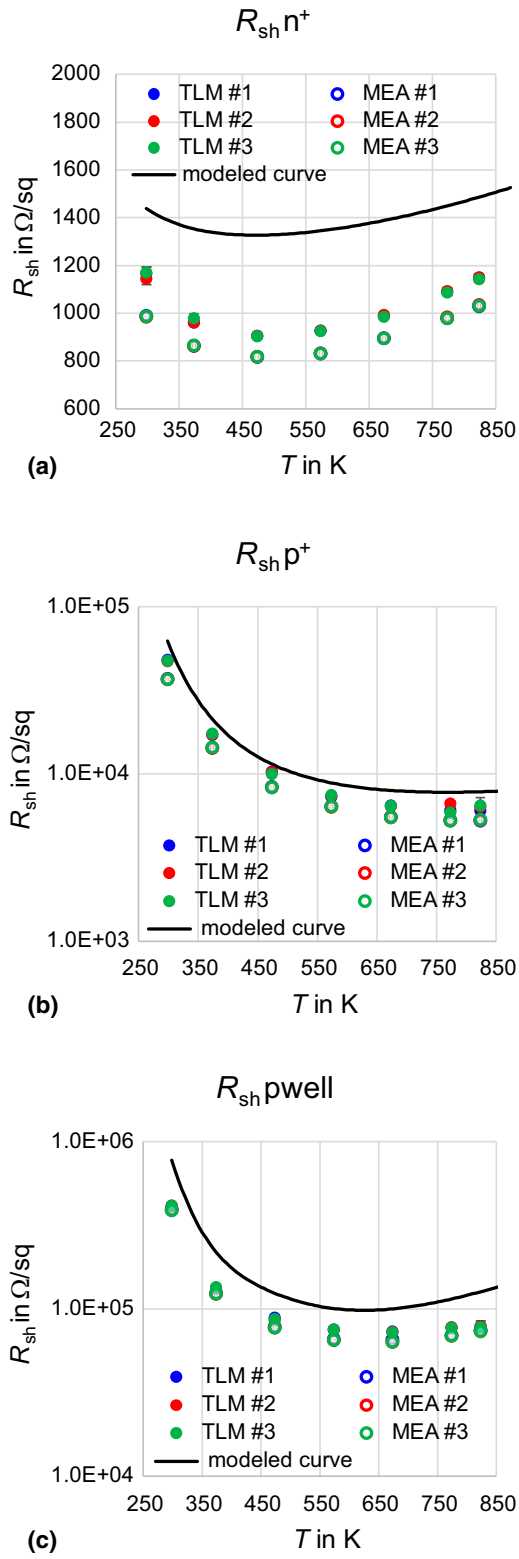

Fig. 4. $R_{sh}(T)$ for (a) n^+, (b) p^+, and (c) pwell implanted regions from both TLM and MEA test structures together with modeled results using parameters given in Table I.

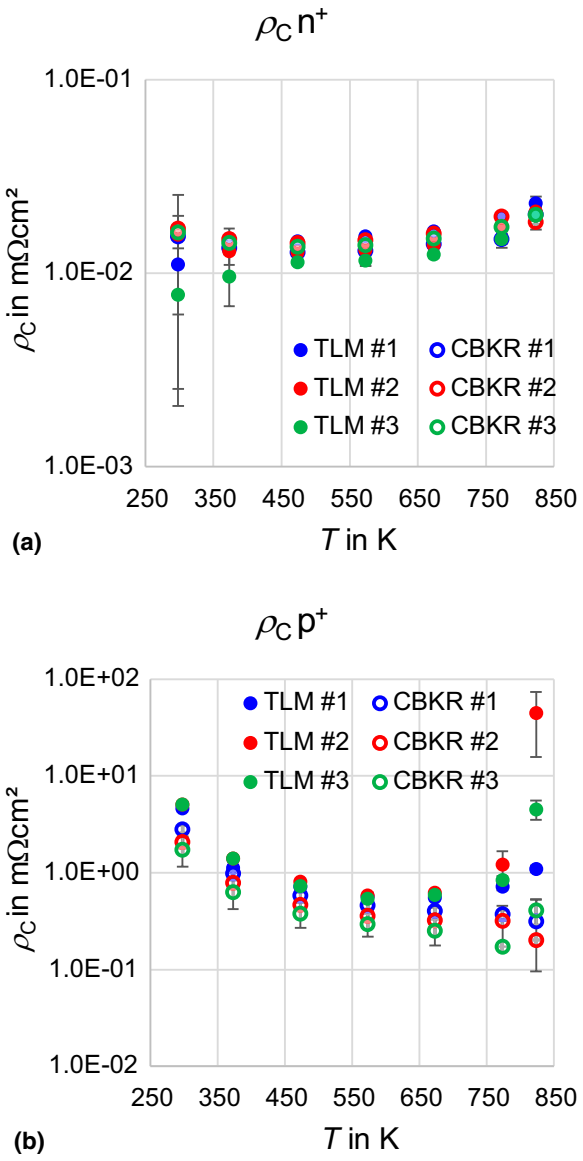

Fig. 5. ρ_c(T) for (a) n^+ and (b) p^+ implanted regions from both TLM and CBKR test structures.

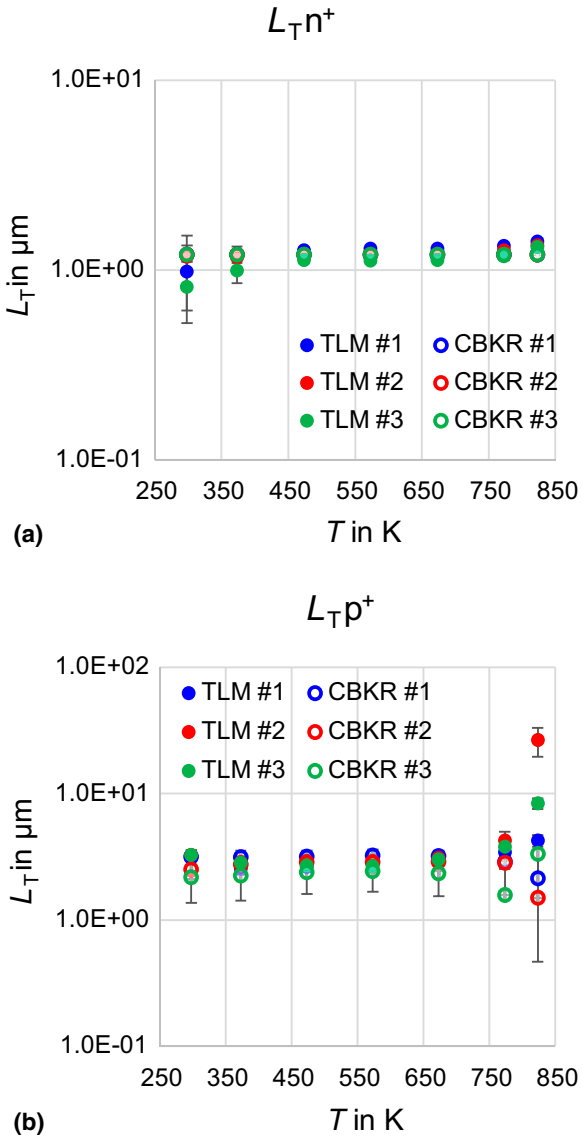

Fig. 6. L_T(T) for (a) n^+ and (b) p^+ implanted regions from both TLM and CBKR test structures.

effective squares length, the contact resistance only contributes 2% of the total MEA resistance.

For contacts on p^+ regions, ρ_c values evaluated by TLM structures show a rather large variation and an increase for measurements at 773 and 823 K which is due to slightly nonideal *R(d)* linearity (i.e., $R^2 < .999$) at those temperatures. For TLM results at lower temperatures as well as for CBKR results, a clear trend of decreasing ρ_c with increasing measurement temperatures can be observed which qualitatively correlates with the according trend for $R_{sh}(T)$ shown in Fig. 4b. It should be noted that only one out of three (3 µm) CBKR contacts for p^+ regions showed ohmic behavior.

Absolute ρ_c values determined for the investigated samples on p^+ regions are rather large compared with values reported in the literature (e.g., [16, 17]) as the contacts on p-type SiC have not fully been optimized yet for the investigated technology. In comparison with the example above for n^+ MEA resistors, the contact resistance of p^+ MEA resistors with the same contact and MEA geometry would give rise to 12% of the total resistance at room temperature.

C. *Sheet Resistance of Metallization and Polycrystalline Silicon*

Evaluated R_{sh} results from MEA test structures for both metallization layers M1 and M2 as well as for polySi, which in principle could also be used as routing layer material are given in Fig. 7 as a function of measurement temperature together with lines fitted according to equation (2) indicating α.

For polySi and M1, two fits for two individual test structures are given which indicate the data variability for the investigated chips whereas for M2 the data from different chips showed very similar resistances for each temperature.

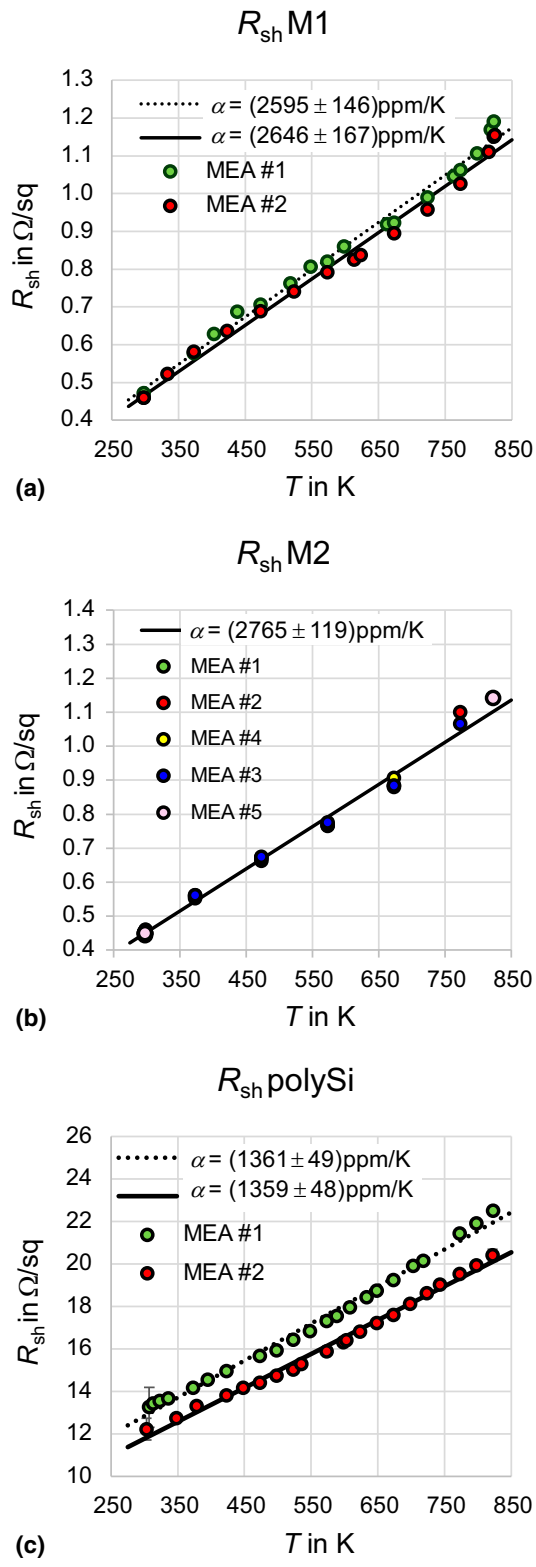

Fig. 7. R_{sh}(T) for (a) M1, (b) M2, and (c) polySi MEA test structures together with lines fitted according to equation (2). Legends give corresponding values of α.

The evaluated α values for both, M1 and M2, resistors are nearly identical considering their uncertainties with a slightly larger value for M2. They are significantly smaller than bulk Pt being used for platinum resistance thermometers which is approximately 3,850 ppm/K for 273-373 K [18]. However, this is expected for thin films attached to substrates with smaller thermal expansion coefficients [19]. For metal stacks consisting of evaporated thin layers of Ti, Pt, and Au with thicknesses of 10, 200, and 50 nm, respectively, a value of (2,977 ± 23) ppm/K was determined for α [20].

The temperature-dependent resistance change observed here for polySi MEA test structures shows a good agreement with data reported in the literature for highly n-doped polysilicon, measured up to 373 K [21].

Conclusions

Relevant ohmic and contact resistances of a 4H-SiC CMOS technology were characterized from room temperature up to 550°C. In a good approximation, a linear temperature dependence could be observed for M1, M2, and polySi resistors, and corresponding values of α were determined. For differently doped 4H-SiC regions, the change of sheet resistances with temperature is qualitatively in agreement with physics-based modeling. Contact resistances to highly doped SiC regions and their temperature dependence were also quantified. Based on these results, the first compact models for these ohmic and contact resistances can be set up and parametrized which supports simplified design optimization of integrated circuits with this technology for operation over a broad range of temperatures.

References

[1] A. May, M. Rommel, L. Baier, M. Schraml, J.F. Dick, M.P.M. Jank, and J. Schulze, "A 4H-SiC CMOS technology enabling smart sensor integration and circuit operation above 500°C," Proceedings of the 2024 Smart Systems Integration Conference and Exhibition (SSI), Hamburg, Germany.

[2] J. Mo, J. Li, Y. Zhang, J. Romijn, A. May, T. Erlbacher, G. Zhang, and S. Vollebregt, "A highly linear temperature sensor operating up to 600°C in a 4H-SiC CMOS technology," *IEEE Electron Device Letters*, Vol. 44, pp. 995-998, 2023.

[3] J. Romijn, S. Vollebregt, L.M. Middelburg, B.E. Mansouri, H.W. van Zeijl, A. May, T. Erlbacher, J. Leijtens, G. Zhang, and P.M. Sarro, "Integrated 64 pixel UV image sensor and readout in a silicon carbide CMOS technology," *Microsystems & Nanoengineering*, Vol. 8, pp. 114, 2022.

[4] EUROPRACTICE IC service, [Online]. https://europractice-ic.com/technologies/compound-semiconductors/fraunhofer-iisb/, accessed June 15, 2024.

[5] D.K. Schroder, *Semiconductor Material and Device Characterization*, 3rd ed., John Wiley & Sons, Inc., Hoboken, New Jersey, 2006.

[6] A. May, L. Baier, and M. Rommel, "Temperature dependence of 4H-SiC gate oxide breakdown and C-V properties from room temperature to 500°C," *Solid State Phenomena*, Vol. 358, pp. 51-58, 2024.

[7] S.J. Proctor, L.W. Linholm, and J.A. Mazer, "Direct measurements of interfacial contact resistance, end contact resistance, and interfacial contact layer uniformity," *IEEE Transactions on Electron Devices*, Vol. 30, pp. 1535-1542, 1983.

[8] T. Johnson, "Passive devices," [Online]. https://faculty-web.msoe.edu/johnsontimoj/EE4981/files4981/passive_devices.pdf, 2019, accessed June 15, 2024.

[9] A. May, M. Rommel, S. Beuer, and T. Erlbacher, "Via size-dependent properties of TiAl ohmic contacts on 4H-SiC," *Materials Science Forum*, Vol. 1062, pp. 185-189, 2022.
[10] H.A. Schafft and J.S. Suehle, "The measurement, use and interpretation of the temperature coefficient of resistance of metallizations," *Solid-State Electronics*, Vol. 35, pp. 403-410, 1992.
[11] J. Weiße, M. Hauck, M. Krieger, A.J. Bauer, and T. Erlbacher, "Aluminum acceptor activation and charge compensation in implanted p-type 4H-SiC," *AIP Advances*, Vol. 9, pp. 055308, 2019.
[12] J. Pernot, S. Contreras, and J. Camassel, "Electrical transport properties of aluminum-implanted 4H–SiC," *Journal of Applied Physics*, Vol. 98, pp. 023706, 2005.
[13] A. Parisini and R. Nipoti, "Analysis of the hole transport through valence band states in heavy Al doped 4H-SiC by ion implantation," *Journal of Applied Physics*, Vol. 114, pp. 243703, 2013.
[14] S. Kagamihara, H. Matsuura, T. Hatakeyama, T. Watanabe, M. Kushibe, T. Shinohe, and K. Arai, "Parameters required to simulate electric characteristics of SiC devices for n-type 4H–SiC," *Journal of Applied Physics*, Vol. 96, pp. 5601-5606, 2004.
[15] I.G. Ivanov, A. Henry, and E. Janzén, "Ionization energies of phosphorus and nitrogen donors and aluminum acceptors in 4H silicon carbide from the donor-acceptor pair emission," *Physical Review B*, Vol. 71, pp. 241201, 2005.
[16] T. Kimoto and J.A. Cooper, *Fundamentals of Silicon Carbide Technology*, John Wiley & Sons, Inc., Singapore, 2014.
[17] F. Roccaforte, M. Vivona, G. Greco, R. Lo Nigro, F. Giannazzo, S. Di Franco, C. Bongiorno, F. Iucolano, A. Frazzetto, S. Rascunà, A. Patti, and M. Saggio, "Ti/Al-based contacts to p-type SiC and GaN for power device applications," *Physica Status Solidi (a)*, Vol. 214, pp. 1600357, 2017.
[18] L Crovini, A Actis, G Coggiola, and A Mangano, "Accurate thermometry by means of industrial platinum resistance thermometers," *Measurement*, Vol. 10, pp. 31-38, 1992.
[19] F. Warkusz, "The size effect and the temperature coefficient of resistance in thin films," *Journal of Physics D: Applied Physics*, Vol. 11, pp. 689-694, 1978.
[20] M. Schepperle, M. Ghanam, A. Bucherer, T. Gerach, and P. Woias, "Non-invasive platinum thin-film microheater/temperature sensor array for predicting and controlling flow boiling in microchannels," *Sensors and Actuators A: Physical*, Vol. 345, pp. 113811, 2022.
[21] M. Boutchich, K. Ziouche, P. Godts, and D. Leclercq, "Characterization of phosphorus and boron heavily doped LPCVD polysilicon films in the temperature range 293-373 K," *IEEE Electron Device Letters*, Vol. 23, pp. 139-141, 2002.